Received: 24 April 2024 | Accepted: 21 October 2025

DOI: 10.1111/mice.70121

INDUSTRIAL APPLICATION

COMPUTER-AIDED CIVIL AND INFRASTRUCTURE ENGINEERING WILEY

Intelligent detection of subsurface road targets using a combined numerical simulation and deep learning method

Hui Yao[1] | **Shuo Pan**[1] | **Yaning Fan**[1] | **Yanhao Liu**[1] | **Gordon Airey**[2] | **Anand Sreeram**[2] | **Yue Hou**[3]

[1]Beijing Key Laboratory of Traffic Engineering, Beijing University of Technology, Beijing, China

[2]Faculty of Engineering, The University of Nottingham, University Park, Nottingham, UK

[3]Department of Civil Engineering, Swansea University, Wales, UK

Correspondence
Hui Yao, College of Metropolitan Transportation, Beijing University of Technology, No.100, Pingleyuan, Chaoyang, Beijing 100124, China.
Email: huiyao@mtu.edu; huiyao@bjut.edu.cn

Yue Hou, Department of Civil Engineering, Swansea University, Wales, UK.
Email: yue.hou@swansea.ac.uk

Funding information
Hunan Expressway Group Co. Ltd., Grant/Award Number: 202152; Hunan Department of Transportation, Grant/Award Number: 202152; Key Scientific Research Projects of BBMG Corporation, Grant/Award Number: KYJC018

Abstract

Detection of subsurface road targets is a crucial task in road engineering. This study focuses on detecting three types of subsurface targets: looseness, pipeline, and voids. Ground-penetrating radar (GPR) was employed to acquire real-world data. gprMax was utilized to generate additional data to address the scarcity of the original dataset. Recognizing the substantial disparity between directly simulated gprMax data and actual GPR images, this paper introduces a novel method for synthesizing gprMax-generated data with real measurements, thereby achieving effective GPR image augmentation. Furthermore, a generative adversarial network (GAN) was employed to rapidly produce large volumes of GPR images. Deep learning models were implemented to detect subsurface road targets using datasets of varying scales. Experimental results indicate that data augmentation utilizing gprMax and GAN can substantially improve the detection accuracy for subsurface road targets, achieving a rate of 0.767. This represents a 21.2% enhancement, compared to the results obtained from training on the original dataset. The findings of this research hold practical significance for supporting road maintenance operations.

1 | INTRODUCTION

1.1 | Underground detection technology

The road contains various subsurface targets, including looseness, pipeline, and voids. Looseness typically results from inadequate compaction or long-term water erosion, which reduces soil density and bearing capacity, potentially leading to road surface subsidence and structural damage. Pipelines feature complex installation layouts and extensive distribution networks. Moreover, incomplete pipeline documentation and complex underground conditions frequently lead to construction-related accidents. Particularly during excavation projects, operational

errors often cause pipeline ruptures, resulting in service interruptions, economic losses, and even public safety incidents. Voids generally form due to soil erosion or leakage from underground pipes, creating empty spaces beneath the pavement that may suddenly collapse under vehicle loads, seriously threatening traffic safety. Therefore, accurate detection of these subsurface targets is essential for ensuring road safety and maintaining structural integrity.

Underground detection techniques include the shallow transient electromagnetic method (Lai et al., 2016) and the high-density electrical method (Z. Huang et al., 2014). In comparison, ground-penetrating radar (GPR) has gained widespread application in the field of underground detection due to its continuous scanning process, high resolution, and non-destructive nature. During the detection process, several key factors require careful consideration. The choice of frequency is related to the radar's detection depth range, and antenna design influences signal strength and resolution, among other factors. The electromagnetic characteristics of underground media exhibit variations that affect the detection outcomes. Therefore, it is necessary to model the electromagnetic parameters under different geological conditions. Extensive research has been conducted on estimating road thickness using radar technology, and the latest studies have accurately inferred the estimation of overlay thickness and reinforcement bar diameter through the integration of radar and electromagnetic induction data (X. Li et al., 2022). In practical detection, the complexity of the environment often leads to low-quality radar data, posing significant challenges for data interpretation. Subjective judgments by technical personnel frequently result in differing interpretations and introduce uncertainties to the conclusions. To enhance the interpretation accuracy of radar, the electromagnetic wave signals of GPR are simulated using the finite-difference time-domain (FDTD) method (Warren et al., 2015). In analogous research, Belli et al. incorporated the dielectric constant of materials into the objective function for the detection of subsurface targets beneath reinforced concrete bridge decks, conducting FDTD simulations (Belli et al., 2008). Their study calculated the difference in simulated amplitude at the boundary versus the actual amplitude on the ground. Despite model-based evaluations, there are still differences between the physical models constructed for simulation and the actual real-world models. Similarly, Cheung and Lai assessed GPR sensitivity to water (Cheung & Lai, 2018). They implemented a field-scale leaking water test to simulate underground water pipe leakage scenarios. By analyzing radar data collected before and after water injection, the researchers identified the leakage points in the water pipes and performed radar wave velocity analysis to validate the ability of radar grayscale images to detect pipe leakage locations.

1.2 | Deep learning techniques for detection

The processing of 2D images has evolved from early-stage techniques, such as threshold segmentation (Al-Amri & Kalyankar, 2010), Sobel (Kanopoulos et al., 1988), and Canny (Er-Sen et al., 2009) edge detection, to machine learning techniques that can extract deep-level features. Rule-based algorithms and electromagnetic wave theories perform well under ideal conditions, but only when external interference is negligible (S. Guo et al., 2022). Machine learning algorithms with multidimensional extraction capabilities significantly enhance detection accuracy and applicability. However, due to the complex transmission background of GPR waves and incomplete feature information extracted, they are challenging to apply comprehensively in detection tasks (Xie et al., 2013). With advancements in hardware and algorithms, intelligent recognition techniques for radar waveform data have advanced significantly. Deep learning, especially after the introduction of the AlexNet (Krizhevsky et al., 2012) neural network model developed for large-scale image recognition, has garnered unprecedented attention, such as earthquake prediction (Rafiei & Adeli, 2017), real estate price estimation (Rafiei & Adeli, 2016), concrete performance prediction (Rafiei et al., 2017), construction cost estimation (Rafiei & Adeli, 2018), detection of pavement cracks (Yao et al., 2024), pavement texture recognition (Pan et al., 2023), and the recognition of railway slab track defects (Cai et al., 2024). The field of object detection has shifted from manual feature design methods to deep learning-based feature extraction techniques. The continuous upgrade of parallel computing resources and the emergence of large-scale publicly available datasets and evaluation metrics have also led to the development of numerous powerful convolutional network models. The emergence of algorithms such as single shot multibox detector (W. Liu et al., 2016), YOLO (you only look once; Bochkovskiy et al., 2020; Redmon et al., 2016; C. Li et al., 2022; C. Y. Wang et al., 2023), fully convolutional one-stage object detection (Tian et al., 2020), and others have propelled the rapid development and widespread application of object detection technology in both academic and industrial domains.

In terms of data preprocessing, a series of data augmentation techniques, such as flipping, mean normalization, scaling, Cutout (DeVries & Taylor, 2017), and Mixup (Zhang et al., 2017), have been introduced to enhance dataset diversity and improve model generalization. For feature fusion and prediction, architectures developed after AlexNet, including Visual Geometry Group (Simonyan & Zisserman, 2014), GoogLeNet (Szegedy et al., 2015), residual network (He et al., 2016),

and DenseNet (densely network) (G. Huang et al., 2017) have advanced computer vision by combining convolutional and non-linear activation layers for complex feature learning. Beyond supervised approaches, unsupervised and semi-supervised methods have also been applied in non-destructive testing. Examples include a Bayesian-optimized unsupervised framework for structural damage localization without predefined feature assumptions (Eltouny & Liang, 2021) and a semi-supervised approach integrating convolutional neural network (CNN) with an uncertainty filter for defect classification using limited labeled data (J. Guo et al., 2021).

The volume of data is crucial for deep learning. However, practical engineering applications often face the issue of limited data availability, making data augmentation highly important. Generative adversarial networks (GANs) are a widely used data augmentation method that leverages adversarial learning between a generator and a discriminator to achieve content generation (Goodfellow et al., 2014). Existing studies have applied GAN in areas such as pavement crack generation (Yao et al., 2024), pavement distress generation (Z. Liu et al., 2023), pavement texture generation (Chen et al., 2022), and railway monitoring signal generation (Y. Wang et al., 2024), demonstrating that GAN-based augmentation can improve detection accuracy.

In recent years, end-to-end object detection techniques have continued to advance, and the integration of deep learning with road radar detection is currently an industry trend. Aydin and Yüksel constructed a model using CNN and employed simulated program-generated radar image data for a classification task (Aydin & Yüksel, 2017). However, the model had a simple architecture, and the dataset consisted of only a small number of images, making it challenging to ensure the model's generalization performance. Due to the limited availability of radar data, Warren et al. acknowledged the strategy proposed by using gprMax (an electromagnetic simulation tool) to address the lack of training data by generating realistic data based on the FDTD principle (Warren et al., 2021). Lu et al. utilized gprMax for numerical simulations of different road defects using GPR (Lu et al., 2022), providing a foundational dataset for radar-based detection of road targets. In an application to improve GPR tunnel lining detection, a self-supervised Mask R-CNN model was fine-tuned with limited labeled data, thereby increasing its accuracy (J. Huang et al., 2024). Chun et al. utilized YOLO and GPR for pipeline detection and employed GAN for data augmentation. Consequently, they achieved an improvement in detection accuracy (Chun et al., 2023).

1.3 | Research objectives and novelty

This study aims to detect subsurface road targets, including looseness, pipeline, and voids, using GPR and deep learning models. The research begins with collecting road information via GPR to establish an original dataset. Subsequently, gprMax simulation is employed to generate new samples containing subsurface road targets, thereby augmenting the original dataset. Building on this, a GAN is employed to further expand the dataset. Finally, a deep learning model is applied to detect subsurface road targets, and the detection performance is compared across datasets of different scales. The technical workflow of this study is shown in Figure 1.

The main contributions of this paper are as follows: (1) It investigates the use of GPR data and deep learning models for detecting subsurface road targets and analyzes the impact of dataset scale on detection performance. (2) A method combining gprMax simulation and image synthesis is proposed to enhance GPR datasets. (3) A GAN-based framework employed for generating realistic GPR images is developed.

2 | GPR DATA COLLECTION AND DATASET ESTABLISHMENT

The road structure was surveyed using GPR. The GPR system was mounted on a trailer towed by a vehicle. An operator drove the vehicle at a constant speed along a predetermined survey line on the road under inspection. The transmitter antenna emitted high-frequency electromagnetic pulses into the road, while the receiver antenna captured reflected signals from interfaces between different material layers (such as the surface layer, base layer, and subgrade) as well as from specific subsurface targets (e.g., looseness, pipeline, and voids) as shown in Figure 2. Each reflection record, known as an A-scan, represents the signal amplitude over time at a single spatial point. A continuous series of A-scans collected along the line forms a 2D radargram, or B-scan, which provides a raw visual profile of the subsurface. In this profile, the horizontal axis corresponds to the distance along the survey line, and the vertical axis represents the two-way travel time of the radar waves.

The raw B-scan data required preprocessing to enhance signal quality and facilitate accurate interpretation. The preprocessing sequence included the following steps: First, we applied background removal to eliminate constant horizontal banding caused by system noise and direct antenna coupling. Next, we performed a time-zero correction to

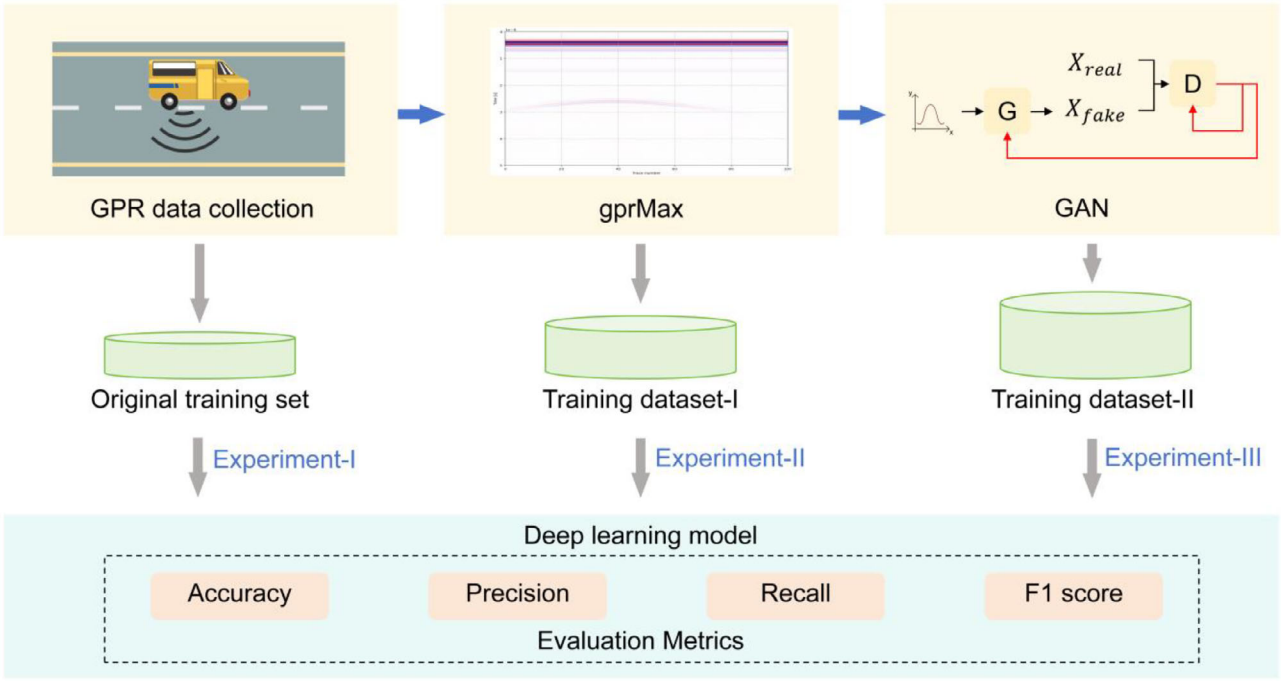

FIGURE 1 Technical workflow of this study. GAN, generative adversarial network; GPR, ground-penetrating radar.

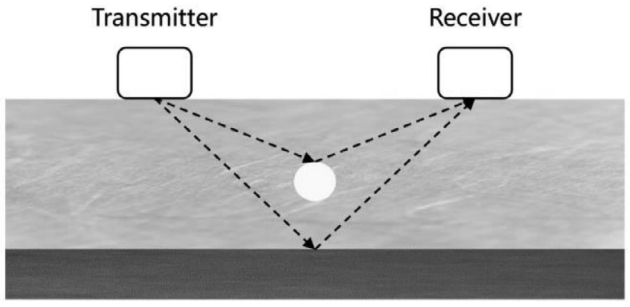

FIGURE 2 Ground-penetrating radar (GPR) transmitting and receiving electromagnetic pulse signals.

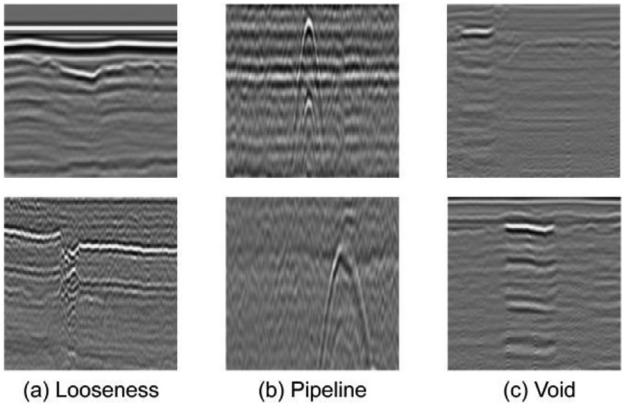

FIGURE 3 Processed GPR B-scan images.

align the start time of all traces. This was followed by bandpass filtering, which removed both low-frequency noise (such as equipment drift) and high-frequency noise (such as electromagnetic interference), while preserving frequency components relevant to the antenna's operating range.

A GPR B-scan is typically an image that is very short in height but extremely wide, making it unsuitable for direct application in target detection algorithms. Therefore, we divided the B-scan image into multiple fixed-size square sub-images. Target detection was then performed by classifying these cropped image patches. To conserve computational resources, each cropped sub-image was resized to 160 ×160 pixels and converted to grayscale as shown in Figure 3. Variations in pixel intensity directly correspond to the strength of radar reflections, providing a consistent representation of the road's internal structure for subsequent automated detection tasks.

Actual radar detection is highly complex due to the intricate nature of underground structures and the varying properties of subsurface media. These factors cause continuous attenuation, reflection, and refraction of electromagnetic waves, which subsequently reduce the resolution and clarity of detected targets. When electromagnetic waves propagate through structural layers with different dielectric constants, reflective interfaces form between these

TABLE 1 Original dataset.

	Looseness	Pipeline	Void	Total
Original training set	140	140	140	420
Test set	60	60	60	180
Total	200	200	200	600

layers according to the principles of wave reflection. In a typical intact structure, these interfaces produce continuous reflection events in radar data. However, the presence of targets (such as looseness, pipeline, and voids) disrupts this continuity. In the resulting grayscale image, signal amplitude is represented by pixel intensity, with brighter areas indicating positive wave peaks and darker areas representing negative wave troughs, thereby making higher-amplitude reflections more visually prominent.

This study collected a total of 600 GPR images, with 200 images for each category: looseness, pipeline, and voids. For each target category, the dataset was divided into training and test sets in a 7:3 ratio, as shown in Table 1. The original training set contained 140 images per category, while the test set contained 60 images per category. During the subsequent data augmentation process, only the training set was augmented, ensuring that the test set was not involved, which effectively mitigated the risk of data leakage.

3 | GPRMAX SIMULATION AND DATA AUGMENTATION

3.1 | gprMax simulation modeling

All electromagnetic phenomena can be described at the macroscopic level using Maxwell's equations. gprMax applies the FDTD algorithm to discretize these equations across temporal and spatial domains, iteratively refining the electromagnetic field distribution for the numerical simulation of wave propagation. Utilizing the principles of FDTD, gprMax can simulate how GPR signals propagate through various media, including phenomena such as reflection and refraction. Due to its flexibility and relatively low computational requirements, the FDTD method is highly suitable for simulating complex scenarios. Additionally, gprMax can leverage the powerful computational capabilities of graphics processing units (GPUs) to significantly accelerate the simulation process.

Based on typical road structures, a model incorporating both the pavement and subgrade was developed. The pavement consists of an upper surface layer with a thickness of 0.15 m and a lower base layer with a thickness of 0.4 m. The underlying subgrade has a thickness of 1.7 m. The looseness, pipeline, and voids investigated in this study are all situated within the subgrade. According to common road material properties, the relative permittivity of the surface layer was set to 4 with a conductivity of 0.001 S/m, while the base layer had a relative permittivity of 9 and a conductivity of 0.002 S/m. The subgrade was assigned a relative permittivity of 12 and a conductivity of 0.005 S/m. The transmitter and receiver antennas were positioned 0.25 m above the surface layer of the pavement, with a horizontal separation of 0.5 m between them. To ensure modeling accuracy, the spatial resolution in all directions was set to 0.005 m.

When conducting forward simulations with gprMax, the type of incident waveform affects the signal penetration capability and the numerical dispersion effects, which directly influence the accuracy and efficiency of the simulation. Typically, GPR employs pulsed electromagnetic waves as the excitation source. The Ricker wavelet, with its peaked oscillatory shape, is commonly used in georadar for detecting shallow targets. It exhibits a prominent peak at the center frequency, making it suitable for detecting targets with distinct reflections. In the following simulations, the Ricker wavelet was employed as the simulated waveform.

The frequency of the excitation source plays a critical role in the detection performance of GPR. A high-frequency source emits shorter wavelengths, offering the advantage of detecting smaller targets and distinguishing closely spaced reflectors. The resulting reflected wave pulses are narrower, with a shorter time window and clearer detail. However, the drawback is rapid signal attenuation and limited penetration depth. In contrast, a low-frequency source exhibits slower attenuation and greater penetration depth, but its longer wavelengths tend to smooth out fine details, making it ineffective for identifying small objects or resolving overlapping echoes from adjacent reflectors. For the road structure inspection task addressed in this study, a frequency of 600 MHz strikes an ideal balance between penetration depth and resolution. Waves in this band, with their moderate wavelength, effectively penetrate the pavement layers to depths of several meters, sufficient to assess the thickness of both the pavement and the subgrade. At the same time, the attenuation rate remains manageable, ensuring the acquisition of valid signals from deeper layers. More importantly, the 600 MHz frequency provides excellent resolution. It generates relatively narrow wavelets capable of clearly identifying centimeter-scale objects within the road structure, such as looseness, pipeline, and voids, while producing radar profiles with distinct layers and well-defined reflective interfaces.

The spatial step size parameter governs the spatial resolution of the numerical model. In gprMax, a B-scan is composed of multiple A-scans. Each A-scan corresponds

to a single step movement of the transmitter and receiver antenna. A higher number of A-scans combined with a smaller step size enhances the resolution of the B-scan, though this comes at the cost of significantly increased computational load. To balance resolution requirements with computational efficiency, this study employed 10 A-scans with a step size of 0.25 m for both transmitter and receiver antennas.

The time window parameter defines the total duration of the simulation, which directly determines the maximum depth detectable by the model. It must be sufficiently long to capture the complete round-trip travel time of the electromagnetic wave from transmission, reflection at a target, and reception. To ensure waveform integrity while conserving computational resources, a time window of 50 ns was selected based on the thickness and relative permittivity of each road layer.

3.2 | Subsurface target configuration

Road looseness often results from water infiltration or repeated traffic loads, leading to reduced bearing capacity and pavement cracking. Particularly critical is looseness occurring between the base course and the subgrade, which is both common and structurally damaging. To simulate this phenomenon numerically, the intrusion of base course material into the subgrade was modeled. In the gprMax simulations, the looseness was represented as a rectangular region within the subgrade, adjacent to the base course. Two geometries were considered: one measuring 0.1 m in width and 0.1 m in depth, and the other 0.1 m in width and 0.05 m in depth. Each looseness configuration was translated laterally across the road cross-section in increments of 0.005 m, resulting in 400 distinct simulated positions per geometry. This methodology generated a total of 800 simulation samples for analysis. An example of the gprMax simulation results for looseness is shown in Figure 4Ia.

Urban underground pipelines are constructed from various materials, selected according to their functional requirements, environmental conditions, and budget constraints. Among these, cast iron pipelines are widely used due to their high strength and corrosion resistance. In the simulations, cast iron pipelines with a radius of 0.3 m were modeled as perfect electric conductors. The pipelines were placed at depths ranging from 0.35 to 1.3 m below the top of the subgrade, with an interval of 0.05 m between successive depths, resulting in 20 distinct depth positions. Along the transverse direction of the road, the pipeline was shifted in steps of 0.05 m, covering 40 transverse positions. In total, 800 gprMax simulations were conducted, each corresponding to a unique pipeline location. An example of the gprMax simulation results for a pipeline is shown in Figure 4Ib.

Voids in road structures typically form due to factors such as water erosion, material fatigue, or inadequate compaction during construction. These voids pose serious threats to road integrity, including reduced load-bearing capacity, accelerated pavement deterioration, and potential sudden collapse. Therefore, the detection of subsurface voids is essential for ensuring road safety and longevity. When a void forms, the original road material is replaced by air or water, resulting in a distinct dielectric contrast that can be identified in GPR signals. In this study, air-filled voids were modeled in simulations, with a relative permittivity of 1 and an electrical conductivity of 0. The void dimensions were set as 0.1 m in both width and depth. In terms of positioning, the depth of the void was varied from 0.25 to 1.2 m below the top of the subgrade, with an interval of 0.05 m, yielding 20 distinct depth levels. Laterally, the void is shifted in 0.05 m steps across the road section, covering 40 transverse positions. In total, 800 unique void configurations were simulated in gprMax to comprehensively analyze their GPR responses. An example of the gprMax simulation results for a void is shown in Figure 4Ic.

3.3 | gprMax data synthesis

Images generated by gprMax cannot be directly used for road detection due to significant discrepancies between simulated and real GPR data, the most critical of which lies in the background characteristics. The simulated images from gprMax exhibit relatively uniform backgrounds, which differ substantially from the complex background information present in actual GPR scans of road structures. It should be emphasized that regardless of whether road materials are modeled as homogeneous or heterogeneous in gprMax, the resulting background fails to resemble that of real scans. This is because the actual distribution of components within the inspected road structure is unknown and cannot be predefined in the simulation.

To address this issue, this study proposes a method for processing and synthesizing gprMax-generated images. First, image cropping was applied. Since the detection targets are all located within the subgrade (i.e., the lower part of the image), the upper quarter of the image, which contains no target information, was removed, retaining only the lower three-quarters. Next, the cropped image was resized to 160 × 160 pixels to match the dimensions of real GPR images. The image was then converted into a single-channel grayscale format as shown in Figure 4II. To enhance the subtle target features in the grayscale image, contrast enhancement was applied using gamma

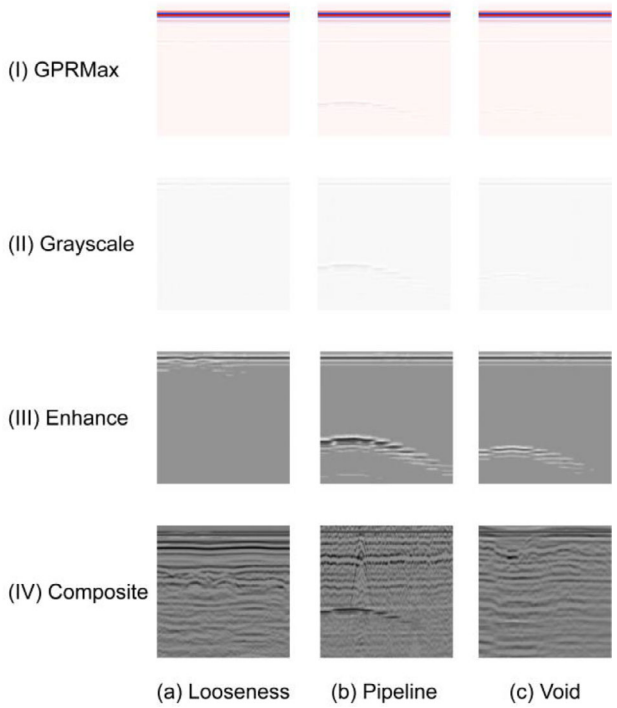

FIGURE 4 Data augmentation using gprMax simulation and synthesis.

correction with a gamma value of 0.05, which improves visibility in darker regions, as illustrated in Figure 4III. Finally, image synthesis was performed. For each gprMax-generated image containing target features, a corresponding image was randomly selected from the training set of real GPR images of the same category. The two images were merged by taking the minimum pixel value at each corresponding position. This synthesis method produces images that retain the target features from the gprMax simulation while incorporating realistic background information similar to that in the original dataset, thereby achieving high-quality data augmentation as shown in Figure 4IV.

Using the proposed gprMax-based image generation and synthesis method, 800 augmented images were created for each of the three target types, specifically looseness, pipeline, and voids, to be used in subsequent detection tasks.

4 | GAN MODELING AND DATA AUGMENTATION

4.1 | GAN modeling

While gprMax enables data augmentation for GPR, this method involves high computational costs and time consumption, as each sample requires individual modeling and simulation. To rapidly generate large volumes of GPR samples, GAN offers an efficient alternative. The key advantage lies in the ability of a trained GAN to produce a substantial number of images quickly, significantly reducing processing time. This capability is of great importance for enhancing the efficiency of road detection workflows.

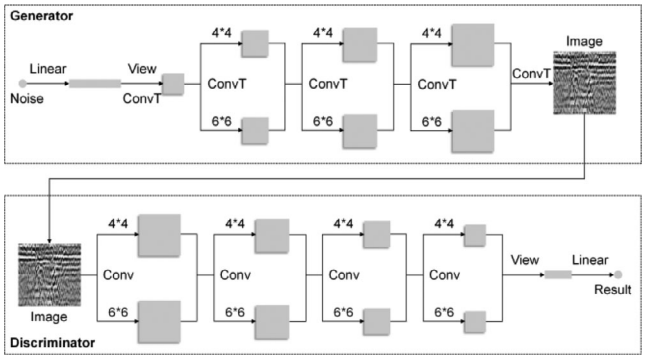

FIGURE 5 Structure of the multi-scale deep convolutional generative adversarial network (MSGAN) generator and discriminator.

GAN is a class of deep learning frameworks specifically developed for unsupervised learning. The architecture consists of two neural networks: a generator and a discriminator, which are pitted against each other in a competitive minimax game. The generator aims to produce synthetic data from random noise that closely mimics real data, while the discriminator functions as a binary classifier. Its task is to distinguish between authentic samples from the true dataset and fabricated ones produced by the generator. Throughout the training process, these two models engage in a dynamic feedback loop. The generator continuously refines its outputs to deceive the discriminator, while the discriminator simultaneously enhances its ability to differentiate between real and generated samples. This adversarial interaction drives iterative improvements in both networks. Upon convergence, the trained generator becomes capable of producing highly realistic images, thereby achieving the goal of data augmentation.

To achieve high-quality augmentation of GPR images, a GAN model was employed. The deep convolutional generative adversarial network (DCGAN; Radford et al., 2015) serves as a widely adopted GAN architecture, recognized for its advantages such as training stability and high-quality image generation. Given the demonstrated importance of multi-scale convolution in enhancing feature extraction capabilities within the field of image processing (Z. Liu et al., 2025; Yan et al., 2025), this study applies a variant of DCGAN, specifically a multi-scale deep convolutional generative adversarial network (MSGAN; Z. Liu et al., 2023), designated for GPR data augmentation. Its structure is illustrated in Figure 5.

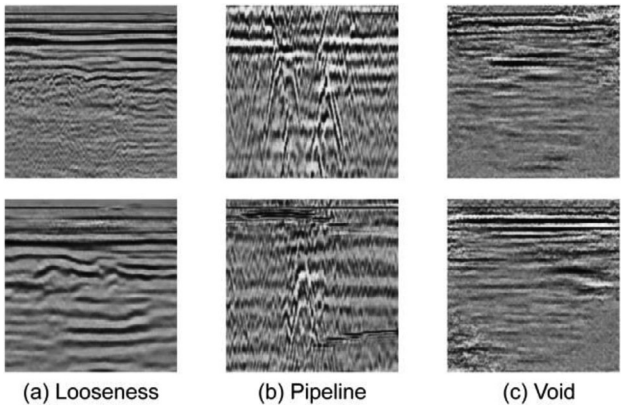

FIGURE 6 Data augmentation using MSGAN.

In the generator of MSGAN, a single noise is used as input. This noise is processed by a linear layer and transformed into a 1D tensor, which is then reshaped and passed through a 1×1 transposed convolution layer to produce a 10×10 feature map. This feature map is separately processed by transposed convolution layers with 4×4 and 6×6 kernels and a stride of 2×2. The resulting outputs are concatenated along the feature dimension to form a 20×20 feature map. Similarly, the feature map undergoes two additional multi-scale transposed convolution stages, resulting in an 80×80 feature map. Finally, this map is processed by a 6×6 transposed convolution layer to generate a 160×160 grayscale image of the road structure.

The discriminator of MSGAN takes a road grayscale image as input. This image is separately processed by convolution layers with 4×4 and 6×6 kernels and a stride of 2×2. The outputs are then concatenated along the feature dimension to form an 80×80 feature map. Subsequently, the feature map passes through three multi-scale convolution layers, reducing its size to 10×10. This feature map is flattened into a 1D vector and fed into a linear layer to produce the final classification result.

4.2 | Data generation

During the training of MSGAN, the Adam optimizer and the binary cross entropy loss function were employed, with the batch size set to 32 and the learning rate set to 0.00001. The training dataset consisted of the original data training set combined with the dataset augmented by gprMax. After 1000 training epochs, the generator of MSGAN was able to produce realistic target images as shown in Figure 6. Using MSGAN, 1000 images were generated for each category of looseness, pipeline, and voids to augment the training set.

MSGAN demonstrates significant advantages in image generation speed. It requires only 3 s to generate 1000 images, which is far more efficient than using gprMax.

TABLE 2 Experimental datasets.

	Looseness	Pipeline	Void	Total
Original training set	140	140	140	420
Training Set—I	940	940	940	2820
Training Set—II	1940	1940	1940	5820
Test set	60	60	60	180

Therefore, for tasks requiring large-scale GPR image generation, the most efficient approach is to first use gprMax to produce a sufficient number of images for MSGAN training and subsequently leverage MSGAN for rapid image generation.

5 | SUBSURFACE TARGETS DETECTION

5.1 | Experimental datasets

The original training set in this study consisted of 140 GPR images per category for looseness, pipeline, and voids. Through gprMax simulation and synthesis, each category was augmented by 800 images, resulting in Training Set I containing 940 images per category. Subsequently, via MSGAN generation, each category was further expanded by 1000 images, yielding a final Training Set-II with 1940 images per category. For both training sets, the testing set remained the original 60 GPR images per category. The detailed composition of the datasets is presented in Table 2.

5.2 | Experimental experiment

The experimental setup was powered by an 11th Gen Intel Core i7-11850H CPU @ 2.50 GHz with 32GB of RAM, and an NVIDIA GeForce RTX 3080 Laptop GPU with 16 GB of dedicated video memory. The programming language used was Python 3.7.3, and the deep learning framework employed was PyTorch 1.12.1 with CUDA 11.3 support.

5.3 | DenseNet model

This study focuses on detecting subsurface road targets through image classification. Due to its superior performance, a DenseNet model was employed for this task (G. Huang et al., 2017). DenseNet is a CNN renowned for its dense connectivity. Its core innovation is the dense block, designed to mitigate the vanishing gradient problem in deep networks and encourage feature reuse. Within each dense block, every layer receives the feature maps of all preceding layers as input, concatenating them along the channel dimension before passing them on.

The standard DenseNet architecture begins with initial convolution and pooling layers, which are followed by a sequence of four dense blocks. Transition layers are inserted between these dense blocks to downsample the feature maps and control model complexity. Each transition layer consists of a batch normalization layer, a 1×1 convolution, and a 2×2 average pooling operation. This work employs the DenseNet-121 variant, which has four dense blocks containing 6, 12, 24, and 16 layers, respectively. Each layer within a block uses a bottleneck structure for computational efficiency. This structure comprises a sequence of operations: batch normalization, a rectified linear unit activation function, a 1×1 convolution, and finally a 3×3 convolution. Consequently, the DenseNet-121 architecture achieves high performance while being more parameter-efficient and computationally effective compared to other networks.

5.4 | Evaluation metrics

The performance of the subsurface target detection model was evaluated on the test set using four key metrics: accuracy, precision, recall, and F1-score. Accuracy measures the proportion of correctly classified samples among the total samples, as defined in Equation (1). Precision indicates the ratio of TP predictions to all samples predicted as positive by the model as given in Equation (2). Recall represents the proportion of actual positive samples that are correctly identified by the model, as expressed in Equation (3). The F1-score is the harmonic mean of precision and recall, calculated according to Equation (4).

$$Accuracy = \frac{TP + TN}{TP + TN + FP + FN} \tag{1}$$

$$Precision = \frac{TP}{TP + FP} \tag{2}$$

$$Recall = \frac{TP}{TP + FN} \tag{3}$$

$$F1\ score = 2 \times \frac{Precision \times Recall}{Precision + Recall} \tag{4}$$

In these formulations, a true positive (TP) denotes a case where the model correctly predicts the positive class; a true negative (TN) refers to a correct prediction of the negative class; a false positive (FP) indicates that the model wrongly predicts the negative class as positive; and a false negative (FN) corresponds to a case where the model fails to predict an actual positive sample.

Furthermore, precision, recall, and F1-score are used to evaluate the detection performance for each individual class, while accuracy is employed to assess the overall detection performance across all classes.

5.5 | Experimental results

The DenseNet model was trained on different training sets, respectively, using the Adam optimizer and cross-entropy loss with a learning rate set to 0.001. The batch size was set to 32 to accelerate training. Training was stopped once the loss function converged. The evaluation metrics of the results corresponding to training sets of different scales on the test set are shown in Table 3.

In Experiment-I, the training set was the original training set, containing 140 images per class. The average accuracy for the three types of targets in the test set was 0.633. Among them, the precision for looseness was relatively high at 0.893, but its recall was low at only 0.417. Consequently, the F1-score for looseness was also low at 0.568. The situation for pipeline was similar to that of looseness, with a high precision of 0.800 but a low recall of 0.533, resulting in a low F1-score of 0.640. In contrast, for void, precision was low at 0.509, while recall was high at 0.950, leading to a low F1-score of 0.663. Overall, the classification performance of Experiment-I for all three target types was poor, struggling to achieve both high precision and high recall simultaneously. As a result, the F1-scores for each category were low, and the average accuracy was also unsatisfactory. This indicates that relying solely on a small amount of real GPR data collected on-site is insufficient for achieving accurate automatic detection of subsurface road targets.

In Experiment-II, the training set was Training Set-I, containing 940 images per class. The average accuracy for the three targets in the test set was 0.711, representing a 12.3% improvement, compared to Experiment-I. In Experiment-II, the precision for looseness reached 1.000, meaning that all results classified as looseness were correct. However, the recall for looseness was extremely low at 0.383, indicating that most instances of looseness were not classified as such. Consequently, the F1-score for looseness was only 0.554. For the pipeline, precision and recall were relatively balanced at 0.742 and 0.767, respectively, yielding an F1-score of 0.754. For void, precision was low while recall was high, at 0.621 and 0.983, respectively. This suggests that although the model correctly classified most instances of void as void, it also misclassified many non-void images as void. The corresponding F1-score was 0.761. Overall, the results of Experiment-II were superior to those of Experiment-I, demonstrating that the gprMax data augmentation and synthesis method proposed in this study positively contributes to improving the accuracy of subsurface road target detection.

In Experiment-III, the training set was training set-II, containing 1940 images per class. The average accuracy for the three targets in the test set was 0.767. The

TABLE 3 Experimental results.

Experiments	Training sets	Categories	Precision	Recall	F1-score	Accuracy
Experiment-I	Original training set	Looseness	0.893	0.417	0.568	0.633
		Pipeline	0.800	0.533	0.640	
		Void	0.509	0.950	0.663	
Experiment-II	Training Set-I	Looseness	1.000	0.383	0.554	0.711
		Pipeline	0.742	0.767	0.754	
		Void	0.621	0.983	0.761	
Experiment-III	Training Set-II	Looseness	0.911	0.683	0.781	0.767
		Pipeline	0.729	0.717	0.723	
		Void	0.711	0.900	0.794	

performance of Experiment-III increased by 21.2%, compared to Experiment-I and by 7.9%, compared to Experiment-II. Specifically, for looseness, precision was 0.911, recall was 0.683, and the F1-score was 0.781. Although precision and recall were not perfectly balanced, extreme disparities were avoided. For the pipeline, precision was 0.729, recall was 0.717, and the F1-score was 0.723, indicating balanced classification performance for this category. For voids, precision was 0.711, recall was 0.900, and the F1-score was 0.794. For this category, recall was higher than precision, but precision was not excessively low. Based on the overall results and the results for each category, the MSGAN data augmentation method proposed in this study further enhances the detection performance for subsurface road targets.

To provide a detailed analysis of the classification outcomes for each category across the experiments, the corresponding confusion matrices are presented in Figure 7. According to Figure 7a, in Experiment-I, 50.0% of the looseness instances and 41.7% of the pipeline instances were misclassified as void. This indicates that the model exhibited a tendency to classify all images as void. The reason for this behavior is likely the limited number of training samples, which made it difficult for the model to accurately learn the distinguishing features of each target category. In Figure 7b, corresponding to Experiment-II, 25.0% of the looseness instances were misclassified as pipeline, while 36.7% were misclassified as void. Additionally, 23.3% of the pipeline instances were misclassified as void. Compared to Experiment-I, Experiment-II reduced the tendency to classify samples as void, and the model demonstrated an improved ability to learn the features of the pipeline category. As shown in Figure 7c, which presents the results of Experiment-III, the misclassification of looseness and pipeline was significantly reduced. Due to the sufficient amount of training data, the model's ability to learn the features of all three categories was enhanced, minimizing confusion to the greatest extent possible.

6 | CONCLUSION

This study focuses on the detection of subsurface road targets, utilizing GPR to acquire internal road structure information and employing deep learning models to identify looseness, pipeline, and voids. To address the issue of insufficient original data, simulations were conducted using gprMax to establish excitation sources and road models, incorporating subsurface targets to obtain GPR images of looseness, pipeline, and void in a simulated environment. Building on this, a method for synthesizing gprMax-generated images with real GPR images was proposed, effectively augmenting the GPR image dataset. To further enhance the dataset on a larger scale, an MSGAN model was employed to enable rapid generation of images representing looseness, pipeline, and voids. DenseNet was used for detection on the original training set and the two augmented training sets to validate the effectiveness of the proposed methods. Experimental results demonstrate that the proposed methods improve the accuracy of subsurface road target detection. The main conclusions of this study are summarized as follows:

1. This study verifies that GPR and DenseNet can be used to detect looseness, pipeline, and voids in road subgrade. GPR leverages the principle that different media reflect waveforms differently, resulting in distinct characteristic B-scan images for various subsurface targets. DenseNet analyzes these targets by learning their unique features, but the classification results are significantly influenced by the volume of data.
2. A GPR data augmentation method based on gprMax is proposed. First, a road model comprising surface layer, base layer, and subgrade is established. Next, an excitation source incorporating frequency, position, and time parameters is defined. Abnormal targets are then embedded within the road model. B-scan images are generated through gprMax simulation. These images are subsequently cropped, compressed, grayscaled, and

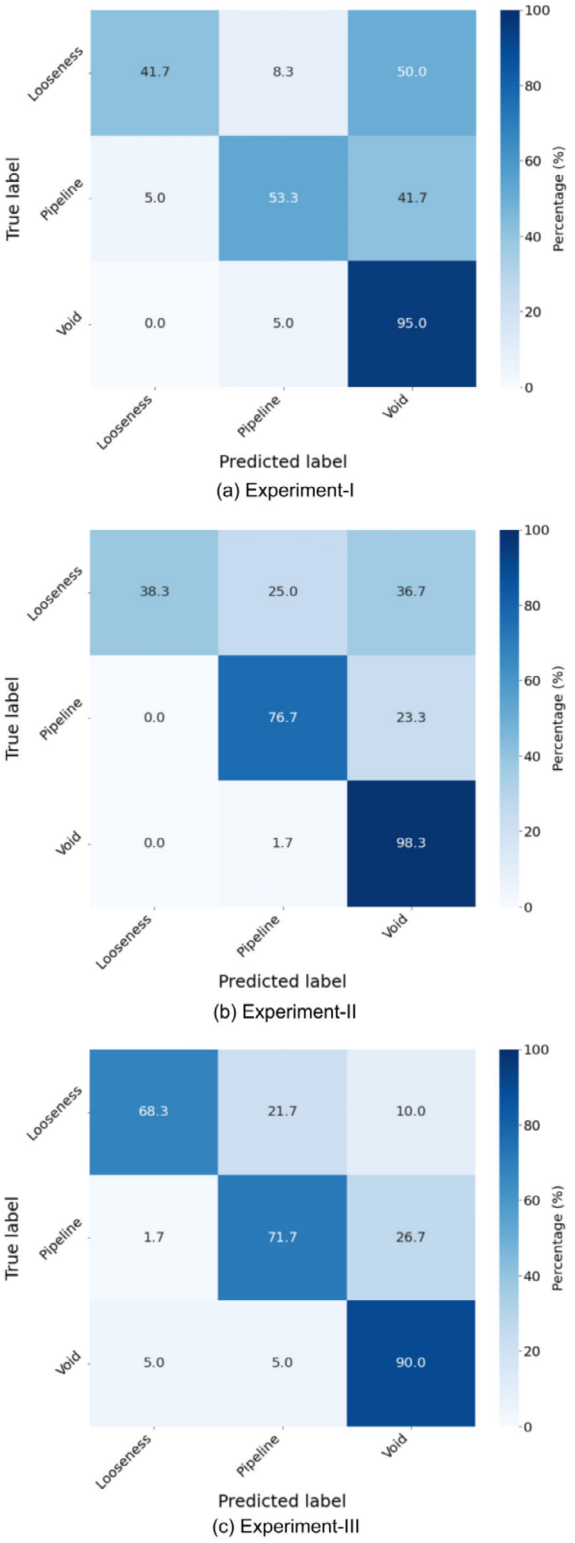

FIGURE 7 Confusion matrices for each experiment.

enhanced in dark regions before being synthesized with original images to achieve GPR data augmentation. Experimental results show that using the gprMax-augmented training set increases the detection accuracy to 0.711, representing a 12.3% improvement over the original training set.

3. An MSGAN-based model is employed for GPR data augmentation. This GAN incorporates multi-scale convolutions in both its generator and discriminator, enabling the generation of GPR images from random noise. The MSGAN was trained on the dataset augmented by gprMax simulations. The trained MSGAN can rapidly and effectively generate GPR images. Experimental results indicate that using the training set augmented by both gprMax and MSGAN achieves a detection accuracy of 0.767, reflecting a 21.2% improvement over the original training set.

The methods proposed in this study effectively enhance the accuracy of subsurface road target detection, holding practical significance for structural health monitoring, construction management, and maintenance in road engineering.

However, the proposed methods have certain limitations. One is that they are primarily applicable to conventional roads, and their generalizability to roads with special materials or unique structures has not been verified. Another is that the study focuses on only three types of subsurface road targets, neglecting other potential facilities or defects within road structures. Additionally, only one type of GAN model was employed, without comparing the enhancement effects of different GAN models on GPR images. Future research will aim to address these limitations.

ACKNOWLEDGMENTS

The authors appreciate the financial support from Hunan Expressway Group Co. Ltd. and the Hunan Department of Transportation (No. 202152) in China. The authors also appreciate the funding support from Key Scientific Research Projects of BBMG Corporation (KYJC018) in China. The authors thank Mr. Zhongjun Xue from Road Engineering Quality Supervision Station of Beijing Municipal and Dr. Zhen Liu from The Chinese University of Hong Kong for their generous help with the data and verification, as well as Mr. Xuyang Zheng from Beijing University of Technology. The large language model Gemini was used for language polishing. Any opinion, finding, and conclusion expressed in this paper are those of the authors and do not necessarily represent the view of any organization.

REFERENCES

Al-Amri, S. S., & Kalyankar, N. V. (2010). *Image segmentation by using threshold techniques*. arXiv Preprint arXiv:1005.4020. https://arxiv.org/abs/1005.4020

Aydin, E., & Yüksel, S. E. (2017). Buried target detection with ground penetrating radar using deep learning method. *2017 25th Signal*

Processing and Communications Applications Conference (SIU), Antalya, Turkey (pp. 1–4).

Belli, K., Wadia-Fascetti, S., & Rappaport, C. (2008). Model based evaluation of bridge decks using ground penetrating radar. *Computer-Aided Civil and Infrastructure Engineering*, *23*(1), 3–16. https://doi.org/10.1111/j.1467-8667.2007.00516.x

Bochkovskiy, A., Wang, C. Y., & Liao, H. Y. M. (2020). *YOLOv4: Optimal speed and accuracy of object detection*. arXiv Preprint arXiv:2004.10934. https://arxiv.org/abs/2004.10934

Cai, X., Tang, X., Pan, S., Wang, Y., Yan, H., Ren, Y., Chen, N., & Hou, Y. (2024). Intelligent recognition of defects in high-speed railway slab track with limited dataset. *Computer-Aided Civil and Infrastructure Engineering*, *39*(6), 911–928. https://doi.org/10.1111/mice.13109

Chen, N., Xu, Z., Liu, Z., Chen, Y., Miao, Y., Li, Q., Hou, Y., & Wang, L. (2022). Data augmentation and intelligent recognition in pavement texture using a deep learning. *IEEE Transactions on Intelligent Transportation Systems*, *23*(12), 25427–25436. https://doi.org/10.1109/TITS.2022.3140586

Cheung, B. W. Y., & Lai, W. W. L. (2018). Field validation of water pipe leak by spatial and time-lapsed measurement of GPR wave velocity. *2018 17th International Conference on Ground Penetrating Radar (GPR)*, Rapperswil, Switzerland (pp. 1–4). https://doi.org/10.1109/ICGPR.2018.8441668

Chun, P. J., Suzuki, M., & Kato, Y. (2023). Iterative application of generative adversarial networks for improved buried pipe detection from images obtained by ground-penetrating radar. *Computer-Aided Civil and Infrastructure Engineering*, *38*(17), 2472–2490. https://doi.org/10.1111/mice.13070

DeVries, T., & Taylor, G. W. (2017). *Improved regularization of convolutional neural networks with cutout*. arXiv Preprint arXiv:1708.04552. https://arxiv.org/abs/1708.04552

Eltouny, K. A., & Liang, X. (2021). Bayesian-optimized unsupervised learning approach for structural damage detection. *Computer-Aided Civil and Infrastructure Engineering*, *36*(10), 1249–1269. https://doi.org/10.1111/mice.12680

Er-Sen, L., Shu-Long, Z., Bao-shan, Z., Yong, Z., Chao-gui, X., & Li-hua, S. (2009). An adaptive edge-detection method based on the Canny operator. *2009 International Conference on Environmental Science and Information Application Technology*, Wuhan, China (pp. 465–469). https://doi.org/10.1109/ESIAT.2009.49

Goodfellow, I. J., Pouget-Abadie, J., Mirza, M., Xu, B., Warde-Farley, D., Ozair, S., Courville, A., & Bengio, Y. (2014). Generative adversarial nets. *Advances in Neural Information Processing Systems*, 27, Montreal, Quebec, Canada.

Guo, J., Wang, Q., & Li, Y. (2021). Semi-supervised learning based on convolutional neural network and uncertainty filter for façade defects classification. *Computer-Aided Civil and Infrastructure Engineering*, *36*(3), 302–317. https://doi.org/10.1111/mice.12632

Guo, S., Xu, Z., Li, X., & Zhu, P. (2022). Detection and characterization of cracks in highway pavement with the amplitude variation of GPR diffracted waves: Insights from forward modeling and field data. *Remote Sensing*, *14*(4), 976. https://doi.org/10.3390/rs14040976

He, K., Zhang, X., Ren, S., & Sun, J. (2016). Deep residual learning for image recognition. *Proceedings of the IEEE Conference on Computer Vision and Pattern Recognition*, Las Vegas, NV (pp. 770–778).

Huang, G., Liu, Z., Van Der Maaten, L., & Weinberger, K. Q. (2017). Densely connected convolutional networks. *Proceedings of the IEEE Conference on Computer Vision and Pattern Recognition*, Honolulu, HI (pp. 4700–4708).

Huang, J., Yang, X., Zhou, F., Li, X., Zhou, B., Lu, S., Ivashov, S., Giannakis, I., Kong, F., & Slob, E. (2024). A deep learning framework based on improved self-supervised learning for ground-penetrating radar tunnel lining inspection. *Computer-Aided Civil and Infrastructure Engineering*, *39*(6), 814–833. https://doi.org/10.1111/mice.13042

Huang, Z., Hu, Y., Zhu, P., & Li, W. (2014). Analysis of resolution influence factors of high-density electrical method and its application. *Journal of Engineering Geology*, *22*(5), 1015–1021.

Kanopoulos, N., Vasanthavada, N., & Baker, R. L. (1988). Design of an image edge detection filter using the Sobel operator. *IEEE Journal of Solid-State Circuits*, *23*(2), 358–367. https://doi.org/10.1109/4.996

Krizhevsky, A., Sutskever, I., & Hinton, G. E. (2012). ImageNet classification with deep convolutional neural networks. *Advances in Neural Information Processing Systems*, 25, Lake Tahoe, NV.

Lai, L., Chen, C., Zhang, H., Bai, C., Su, Z., Jia, H., Xiao, M., & Hou, H. (2016). Application of shallow transient electromagnetic method in the detection of city road disease. *Progress in Geophysics*, *31*(6), 2743–2746.

Li, C., Li, L., Jiang, H., Weng, K., Geng, Y., Li, L., Ke, Z., Li, Q., Cheng, M., Nie, W., Li, Y., Zhang, B., Liang, Y., Zhou, L., Xu, X., Chu, X., Wei, X., & Wei, X. (2022). *YOLOv6: A single-stage object detection framework for industrial applications*. arXiv preprint arXiv:2209.02976. https://arxiv.org/abs/2209.02976

Li, X., Liu, H., Zhou, F., Chen, Z., Giannakis, I., & Slob, E. (2022). Deep learning–based nondestructive evaluation of reinforcement bars using ground-penetrating radar and electromagnetic induction data. *Computer-Aided Civil and Infrastructure Engineering*, *37*(14), 1834–1853. https://doi.org/10.1111/mice.12798

Liu, W., Anguelov, D., Erhan, D., Szegedy, C., Reed, S., Fu, C. Y., & Berg, A. C. (2016). SSD: Single shot multibox detector. *European Conference on Computer Vision*, Amsterdam, The Netherlands (pp. 21–37).

Liu, Z., Pan, S., Gao, Z., Chen, N., Li, F., Wang, L., & Hou, Y. (2023). Automatic intelligent recognition of pavement distresses with limited dataset using generative adversarial networks. *Automation in Construction*, *146*, 104674. https://doi.org/10.1016/j.autcon.2022.104674

Liu, Z., Zhang, E., Pan, S., Li, S., Long, Y., & Witlox, F. (2025). Assessing urban emergency medical services accessibility for older adults considering ambulance trafficability using a deep learning approach. *Sustainable Cities and Society*, *132*, 106804 https://doi.org/10.1016/j.scs.2025.106804

Lu, S. T., Yuan, J. Y., Chen, M., Mao, X. R., & Wang, J. H. (2022). Numerical simulation of ground-penetrating radar based on GprMax for the road disease. In T.-H. Law & B. Guo (Eds.), *Frontier research: Road and traffic engineering*, CRC Press (pp. 141–147). https://doi.org/10.1201/9781003305002

Pan, S., Yan, H., Liu, Z., Chen, N., Miao, Y., & Hou, Y. (2023). Automatic pavement texture recognition using lightweight few-shot learning. *Philosophical Transactions of the Royal Society A*, *381*(2254), 20220166. https://doi.org/10.1098/rsta.2022.0166

Radford, A., Metz, L., & Chintala, S. (2015). *Unsupervised representation learning with deep convolutional generative adversarial*

networks. arXiv preprint arXiv:1511.06434. https://arxiv.org/abs/1511.06434

Rafiei, M. H., & Adeli, H. (2016). A novel machine learning model for estimation of sale prices of real estate units. *Journal of Construction Engineering and Management*, *142*(2), 04015066. https://doi.org/10.1061/(ASCE)CO.1943-7862.0001047

Rafiei, M. H., & Adeli, H. (2017). NEEWS: A novel earthquake early warning model using neural dynamic classification and neural dynamic optimization. *Soil Dynamics and Earthquake Engineering*, *100*, 417–427. https://doi.org/10.1016/j.soildyn.2017.05.013

Rafiei, M. H., & Adeli, H. (2018). Novel machine-learning model for estimating construction costs considering economic variables and indexes. *Journal of Construction Engineering and Management*, *144*(12), 04018106. https://doi.org/10.1061/(ASCE)CO.1943-7862.0001570

Rafiei, M. H., Khushefati, W. H., Demirboga, R., & Adeli, H. (2017). Supervised deep restricted Boltzmann machine for estimation of concrete. *ACI Materials Journal*, *114*(2), 237. https://doi.org/10.14359/51689560

Redmon, J., Divvala, S., Girshick, R., & Farhadi, A. (2016). You only look once: Unified, real-time object detection. *2016 IEEE Conference on Computer Vision and Pattern Recognition (CVPR)*, Las Vegas, NV (pp. 779–788). https://doi.org/10.1109/CVPR.2016.91

Simonyan, K., & Zisserman, A. (2014). Very deep convolutional networks for large-scale image recognition. arXiv Preprint arXiv:1409.1556. https://arxiv.org/abs/1409.1556

Szegedy, C., Liu, W., Jia, Y., Sermanet, P., Reed, S., Anguelov, D., Erhan, D., Vanhoucke, V., & Rabinovich, A. (2015). Going deeper with convolutions. *Proceedings of the IEEE Conference on Computer Vision and Pattern Recognition*, Boston, MA (pp. 1–9).

Tian, Z., Shen, C., Chen, H., & He, T. (2020). FCOS: A simple and strong anchor-free object detector. *IEEE Transactions on Pattern Analysis and Machine Intelligence*, *44*(4), 1922–1933.

Wang, C. Y., Bochkovskiy, A., & Liao, H. Y. M. (2023). YOLOv7: Trainable bag-of-freebies sets new state-of-the-art for real-time object detectors. *Proceedings of the IEEE/CVF Conference on Computer Vision and Pattern Recognition*, Vancouver, BC, Canada (pp. 7464–7475).

Wang, Y., Cai, X., Tang, X., Pan, S., Wang, Y., Yan, H., Ren, Y., & Hou, Y. (2024). HSRA-Net: Intelligent detection network of anomaly monitoring data in high-speed railway. *IEEE Transactions on Intelligent Transportation Systems*, *25*(12), 20793–20803. https://doi.org/10.1109/TITS.2024.3477752

Warren, C., Giannakis, I., & Giannopoulos, A. (2021). gprMax: An open source electromagnetic simulator for generating big data for ground penetrating radar applications. *EGU General Assembly 2021*, Virtual.

Warren, C., Giannopoulos, A., & Giannakis, I. (2015). An advanced GPR modelling framework: The next generation of gprMax. *2015 8th International Workshop on Advanced Ground Penetrating Radar (IWAGPR)*, Florence, Italy (pp. 1–4).

Xie, X., Li, P., Qin, H., Liu, L., & Nobes, D. C. (2013). GPR identification of voids inside concrete based on the support vector machine algorithm. *Journal of Geophysics and Engineering*, *10*(3), 034002. https://doi.org/10.1088/1742-2132/10/3/034002

Yan, H., Pan, S., Zhang, S., Wu, F., & Hao, M. (2025). Sustainable utilization of road assets concerning obscured traffic signs recognition. *Proceedings of the Institution of Civil Engineers-Engineering Sustainability*, *178*(2), 124–134. https://doi.org/10.1680/jensu.24.00090

Yao, H., Liu, Y., Lv, H., Huyan, J., You, Z., & Hou, Y. (2024). Encoder-decoder with pyramid region attention for pixel-level pavement crack recognition. *Computer-Aided Civil and Infrastructure Engineering*, *39*(10), 1490–1506. https://doi.org/10.1111/mice.13128

Yao, H., Wu, Y., Liu, S., Liu, Y., & Xie, H. (2024). A pavement crack synthesis method based on conditional generative adversarial networks. *Mathematical Biosciences and Engineering*, *21*(1), 903–923. https://doi.org/10.3934/mbe.2024038

Zhang, H., Cisse, M., Dauphin, Y. N., & Lopez-Paz, D. (2017). *mixup: Beyond empirical risk minimization*. arXiv Preprint arXiv:1710.09412. https://arxiv.org/abs/1710.09412

How to cite this article: Yao, H., Pan, S., Fan, Y., Liu, Y., Airey, G., Sreeram, A., & Hou, Y. (2025). Intelligent detection of subsurface road targets using a combined numerical simulation and deep learning method. *Computer-Aided Civil and Infrastructure Engineering*, 1–13. https://doi.org/10.1111/mice.70121